MNRAS **000**, 1–13 (2016) Preprint 26 January 2017 Compiled using MNRAS LATEX style file v3.0

Cold dark energy constraints from the abundance of galaxy clusters

Caroline Heneka[1,2⋆], David Rapetti[1,3,4,5,6], Matteo Cataneo[1,7], Adam B. Mantz[8,9], Steven W. Allen[8,9,10], Anja von der Linden[1,8,9,11]

[1] *Dark Cosmology Center, Niels Bohr Institute, University of Copenhagen, Juliane Maries Vej 30, 2100 Copenhagen, Denmark*
[2] *Department of Physics & Astronomy, University of California, Irvine, CA 92697*
[3] *Faculty of Physics, Ludwig-Maximilians-Universität, Scheinerstr. 1, 81679 Munich, Germany*
[4] *Excellence Cluster Universe, Boltzmannstr. 2, 85748 Garching, Germany*
[5] *Center for Astrophysics and Space Astronomy, Department of Astrophysical and Planetary Science, University of Colorado, Boulder, C0 80309, USA*
[6] *NASA Ames Research Center, Moffett Field, CA 94035, USA*
[7] *Institute for Astronomy, University of Edinburgh, Royal Observatory, Blackford Hill, Edinburgh, EH9 3HJ, U.K.*
[8] *Kavli Institute for Particle Astrophysics and Cosmology, Stanford University, 452 Lomita Mall, Stanford, CA 94305, USA*
[9] *Department of Physics, Stanford University, 382 Via Pueblo Mall, Stanford, CA 94305, USA*
[10] *SLAC National Accelerator Laboratory, 2575 Sand Hill Road, Menlo Park, CA 94025, USA*
[11] *Department of Physics and Astronomy, Stony Brook University, Stony Brook, NY 11794, USA*

arXiv:1701.07319v1 [astro-ph.CO] 25 Jan 2017

Accepted XXX. Received YYY; in original form ZZZ

ABSTRACT

We constrain cold dark energy of negligible sound speed using observations of the abundance of galaxy clusters. In contrast to standard quasi-homogeneous dark energy, negligible sound speed implies clustering of the dark energy fluid at all scales, allowing us to measure the effects of dark energy perturbations at cluster scales. We compare both models and set the stage for using non-linear information from semi-analytical modelling in cluster growth data analyses. For this, we re-calibrate the halo mass function with non-linear characteristic quantities, the spherical collapse threshold and virial overdensity, that account for model and redshift dependent behaviours, as well as an additional mass contribution for cold dark energy. We present the first constraints from this cold dark matter plus cold dark energy mass function using our cluster abundance likelihood, which self-consistently accounts for selection effects, covariances and systematic uncertainties. We also combine these cluster results with other probes using CMB, SNe Ia and BAO data, and find a shift between cold versus quasi-homogeneous dark energy of up to 1σ. We then employ a Fisher matrix forecast of constraints attainable with cluster growth data from on-going and future surveys. For the Dark Energy Survey, we obtain ∼50% tighter constraints for cold dark energy compared to those of the standard model. In this study we show that cluster abundance analyses are sensitive to cold dark energy, an alternative viable model that should be routinely investigated alongside the standard dark energy scenario.

Key words: cosmology: observations – cosmology: theory – large-scale structure of universe – galaxies: clusters: general – dark energy

1 INTRODUCTION

Cosmology has entered a phase where more and more precise measurements enable us to put increasingly tight constraints on model parameters. Since evidence was found for late-time accelerated expansion (Riess et al. 1998; Perlmutter et al. 1999), the possibility of either a cosmological constant, dynamical dark energy or modifications of gravity has been a question central to cosmology (for reviews see e.g. Copeland et al. 2006; De Felice & Tsujikawa 2010; Clifton et al. 2012; Joyce et al. 2015). To guarantee the accuracy of such precise constraints, our modelling toolkit needs to be extended. For this, it is key to explore a wider range of model and parameter spaces, while correctly translating model charac-

⋆ E-mail: caroline@dark-cosmology.dk

© 2016 The Authors

teristics into quantities testable against data. The objective is to maximise the information gain and to not overlook distinctive signatures.

Both in the linear and non-linear regimes, galaxy cluster surveys are highly competitive probes of cosmological models and fundamental physics. This has been shown in results ranging from estimating standard cosmological parameters (Mantz et al. 2008; Vikhlinin et al. 2009; Mantz et al. 2010a; Rozo et al. 2010; Allen et al. 2011; Benson et al. 2013; Mantz et al. 2014, 2015; Applegate et al. 2016) to constraining non-Gaussianities of primordial density fluctuations (Sartoris et al. 2010a; Shandera et al. 2013; Mana et al. 2013) and testing predictions of General Relativity and modified gravity scenarios (Schmidt et al. 2009a; Rapetti et al. 2010; Lombriser et al. 2012; Rapetti et al. 2013; Cataneo et al. 2015). The high mass end of the halo mass function, which can be constrained by observations of galaxy clusters, is particularly sensitive to cosmological models through both the background evolution and the linear and non-linear growth of structure formation. For a vanilla model with a cosmological constant and cold dark matter (ΛCDM), the halo mass function has been carefully modelled and calibrated (Sheth & Tormen 1999; Tinker et al. 2008; Jenkins et al. 2001; Maggiore & Riotto 2010; Tinker et al. 2010; Corasaniti & Achitouv 2011; Despali et al. 2016; Bocquet et al. 2016). Beyond this standard assumption, continued efforts have been directed to modelling the mass function for extended theories (Schmidt et al. 2009b; Bhattacharya et al. 2011; Cui et al. 2012; Barreira et al. 2013; Kopp et al. 2013; Cataneo et al. 2016). For some models beyond ΛCDM, dark energy can be effectively parametrized as a fluid with an equation of state, w, and a sound speed of perturbations, c_s^2. For dynamical dark energy models, a sound speed different from one (speed of light), even time- and scale-dependent, is quite natural. One of the simplest examples for dark energy models with a varying sound speed is Quintessence with non-canonical kinetic terms, known as K-essence (Armendariz-Picon et al. 1999; Armendariz-Picon et al. 2000).

First attempts to constrain the sound speed of dark energy at the linear level came from Weller & Lewis (2003) using cosmic microwave background (CMB), large scale structure (LSS) and supernova data, Bean & Doré (2004) using CMB and CMB LSS cross correlation data, and Hannestad (2005) using CMB, galaxy clustering and weak lensing data. Later on, Abramo et al. (2009) forecasted such measurements from galaxy cluster number counts as did Appleby et al. (2013), but for the combination of these with CMB data sets, and Hojjati & Linder (2016) studied the potential use of CMB lensing data for this purpose. Creminelli et al. (2010b) and Batista & Pace (2013) extended the analysis of dark energy models with negligible sound speed to the non-linear level of structure formation utilizing the spherical collapse formalism. Basse et al. (2011) and Basse et al. (2014) followed a similar approach but for dark energy models with an arbitrary speed of sound, and also forecasted parameter constraints.

The goal of this paper is to capture the rich non-linear information of structure formation enclosed into our cluster growth data. For this, we implement a semi-analytical framework that incorporates the dominant effects of cold dark energy into the halo mass function. Using this data analysis, we present the first observational constraints on cold (clustering) dark energy ($c_s^2 = 0$). We also compare these results with those for quasi-homogeneous dark energy ($c_s^2 = 1$) to investigate the impact of the common assumption of $c_s^2 = 1$ when constraining w and the other relevant standard parameters (see Section 5). We also then study the difference between constraints on these two models from upcoming cluster measurements such as those from the Dark Energy Survey (see Section 6).

This paper is organised as follows. Section 2 describes the semi-analytical framework we use to calculate the non-linear model characteristics of interest for both cold and quasi-homogeneous dark energy, and illustrates their behaviour. In Section 3 we proceed to re-calibrate the halo mass function with these non-linear quantities. Section 4 briefly describes the data we use to constrain cosmological parameters. In Section 5 we present our results on standard cosmological parameters for both cold and quasi-homogeneous dark energy, and in Section 6 we forecast such constraints for ongoing and upcoming surveys. We summarise our findings and discuss the broader implications in Section 7.

2 NON-LINEAR CHARACTERISTICS

In this section we review the effects of assuming cold dark energy on non-linear quantities such as the cosmology-dependent linear threshold of collapse, the virial overdensity, and the cold dark energy mass contribution to virialised objects. We use the spherical collapse formalism to calculate the perturbations stemming from dark energy being clustering instead of quasi-homogeneous. This enables us to re-calibrate the cluster mass function for cold dark energy by implementing into it these non-linear quantities.

Cold dark energy designates a dark energy fluid whose sound speed is extremely low, i.e. approaching the limit of zero sound speed. Dark energy fluids of sound speed smaller than one are obtained for example in Quintessence theories with non-canonical kinetic terms known as K-essence (Armendariz-Picon et al. 2000). Also, in Quintessence zero sound speed is required for co-called phantom values of the equation of state, or a phantom crossing (Creminelli et al. 2009). In the following we will assume a dark energy fluid with an effective sound speed c_s^2 and equation of state w, at the limits where $c_s^2 \to 0$ for cold dark energy and $c_s^2 = 1$, i.e. the speed of light, for quasi-homogeneous dark energy. The effective sound speed is defined here as $c_s^2 = \delta p_e / \delta \rho_e$, with δp_e and $\delta \rho_e$ being the pressure and density perturbations of the dark energy fluid, respectively (Hu & Eisenstein 1999). This relation is more general than that of the adiabatic sound speed c_a^2, where $c_s^2 = c_a^2$ only for perfect fluids. We restrict our current analysis to an effective constant equation of state $w = p_e/\rho_e$, where p_e is the pressure and ρ_e the energy density of the fluid. In addition, we assume negligible anisotropic stress and a flat Friedmann-Lemaître-Robertson-Walker (FLRW) background.

2.1 Fluid equations and spherical collapse

Here we describe the set of equations we employ within the spherical collapse framework to derive the non-linear quan-

tities needed to re-calibrate the halo mass function in Section 3.

The background evolution is governed by the first Friedmann equation in the presence of dark matter and dark energy fluids, $H^2(a) = H_0^2\left[\Omega_{\mathrm{m},0}a^{-3} + \Omega_{\mathrm{de},0}e^{-3(1+w)}\right]$, with $\Omega_{\mathrm{m},0}$ and $\Omega_{\mathrm{de},0}$ being the present-day mean matter and dark energy densities, and H_0 the Hubble constant. We neglect the impact of baryons and radiation, with baryons being an extra minor matter contribution in this setup and radiation being negligible at the late times relevant for this study. The continuity and Euler equation read

$$\frac{\partial \rho_I}{\partial t} + \nabla_r \cdot (\rho_I + p_I)\, v_I = 0\,, \tag{1}$$

$$\frac{\partial v_I}{\partial t} + (v_I \cdot \nabla_r)\, v_I + \frac{\nabla_r p_I + v_I \dot{p}_I}{\rho_I + p_I} + \nabla_r \Phi = 0\,, \tag{2}$$

with density ρ_I, three-velocity v_I and pressure p_I for each species I, with Φ denoting the Newtonian potential. At late times, all scales relevant for structure formation are well within the horizon and we can safely take the Newtonian limit of the fluid equations (1) and (2). Moreover, to investigate the non-linear evolution of density fluctuations we expand the fluid quantities, both for dark matter and dark energy (Pace et al. 2010, 2014). Fluctuations in density δ_I and pressure δp_I, as well as the peculiar velocity u_I, are defined for each species I through $\rho_I = \bar{\rho}_I(1+\delta_I)$, $p_I = \bar{p}_I + \delta p_I$, and $v_I = a[H(a)x + u_I]$, respectively, where x is the comoving coordinate and overbars denote the corresponding background quantities. For fluids with constant sound speed $c_{\mathrm{s},I}$ and constant equation of state w_I, the corresponding equations for density perturbations and velocity potential $\theta_I = (\nabla_x \cdot u)_I$ in the Newtonian limit read

$$\dot{\delta}_I + 3H\left(c_{\mathrm{s},I}^2 - w_I\right)\delta_I + \frac{\theta_I}{a}\left[(1+w_I) + \left(1 + c_{\mathrm{s},I}^2\right)\delta_I\right] = 0\,, \tag{3}$$

$$\dot{\theta}_I + 2H\theta_I + \frac{\theta_I^2}{3a} = \nabla^2\Phi\,. \tag{4}$$

The Poisson equation describes how the potential Φ is sourced by the density and pressure perturbations, that is

$$\nabla^2\Phi = -4\pi G \sum_I \left(1 + 3c_{\mathrm{s},I}^2\right) a^2 \bar{\rho}_I \delta_I\,, \tag{5}$$

where the sum runs over each species considered, here dark matter and dark energy. In the case of quasi-homogeneous dark energy with $c_{\mathrm{s}} = 1$, the non-linear equations and their linearised counterparts are taken in the limit of negligible dark energy perturbations with $\delta_{\mathrm{de}} \to 0$ for the system of coupled equations (3)–(5), neglecting large-scale modes. For cold dark energy with $c_{\mathrm{s}} \to 0$ we have negligible dark energy pressure perturbations $\delta p_{\mathrm{de}} \ll \delta\rho_{\mathrm{de}}$, since $\delta p_{\mathrm{de}} = c_{\mathrm{s}}^2 \delta\rho_{\mathrm{de}}$.

For cold dark energy, the combination of the linearised version of equations (3)-(5) for dark matter and dark energy gives

$$\begin{aligned} &\ddot{\delta}_{\mathrm{m}} + 2H\dot{\delta}_{\mathrm{m}} = 4\pi G(\bar{\rho}_{\mathrm{m}}\delta_{\mathrm{m}} + \bar{\rho}_{\mathrm{de}}\delta_{\mathrm{de}}) \\ &\dot{\delta}_{\mathrm{de}} - 3Hw\delta_{\mathrm{de}} = (1+w)\,\dot{\delta}_{\mathrm{de}}\,. \end{aligned} \tag{6}$$

Initial conditions are chosen during matter domination when $\delta_{\mathrm{m}} \propto a$ holds. The initial dark energy contrast $\delta_{\mathrm{de},i}$ can be expressed in terms of the dark matter density contrast $\delta_{\mathrm{m},i}$ as

$$\delta_{\mathrm{de},i} = \frac{1+w}{1-3w}\,\delta_{\mathrm{m},i}\,, \tag{7}$$

and $\dot{\delta}_{\mathrm{m},i} = H(a_i)\,\delta_{\mathrm{m},i}$ at the initial scale factor a_i.

As stated, we want to derive the non-linear quantities that describe the cosmology-dependent formation of bound structures within the spherical collapse framework. These are the density threshold of collapse, the overdensity at virialisation and a cold dark energy mass contribution to the bound objects. Their behaviour will be discussed in detail in the following Sections from 2.2 to 2.4. To compute these quantities, for dark energy and dark matter we evolve the set of coupled non-linear equations (3)-(5) and their linearisation using equation (7) for both standard quasi-homogeneous dark energy with sound speed $c_{\mathrm{s}}^2 = 1$ and cold dark energy with $c_{\mathrm{s}}^2 = 0$. The evolution of the non-linear equations determines the point of collapse, defined as the singularity where the non-linear matter density perturbation diverges. The solution of the linear equations at the time of collapse gives then the linear threshold of collapse. And the solutions of the non-linear equations at the time of virialisation provide us with the virial overdensity and the dark energy mass contribution at virialisation. The initial dark matter density contrast $\delta_{\mathrm{m},i}$ is adjusted such that the point of collapse takes place at low redshifts of interest.

The point of collapse for an overdensity is reached when the non-linear matter density perturbation diverges. This corresponds to tracking the evolution of a spherical homogeneous top-hat overdensity of radius R until its radius reaches zero, i.e. the point of collapse. For Birkhoff's theorem, this is equivalent to the evolution of a separate closed FLRW universe where the scale factor a is replaced by a distinct scale factor R within the overdensity. The radius evolution of the spherical overdensity is obtained from the isotropic and homogeneous solution of the Euler equation (2) in the Hubble flow $v = Hx$, which corresponds to $\ddot{a}/a = -\nabla\Phi$ with the scale factor a replaced by the radius R and inserting the gradient potential $\nabla\Phi = (4\pi G/3)\sum(\rho_I + 3p_I)x$. Hence, the evolution of the spherical overdensity in the presence of cold dark energy is described by (Creminelli et al. 2010a)

$$\frac{\ddot{R}}{R} = -\frac{4\pi G}{3}\left(\rho_{\mathrm{m}} + \rho_{\mathrm{de}} + 3\bar{p}_{\mathrm{de}}\right), \tag{8}$$

where we have used $\delta p_{\mathrm{de}} \approx 0$. For quasi-homogeneous dark energy with $c_{\mathrm{s}} = 1$ we have $\rho_{\mathrm{de}} = \bar{\rho}_{de}$. For the evolution of the dark matter and dark energy densities within a spherical overdensity of radius R, the continuity equation (1) gives

$$\dot{\rho}_I + 3\frac{\dot{R}}{R}(\rho_I + p_I) = 0\,. \tag{9}$$

In order to solve for collapse, equations (8) and (9) are evolved until a singularity is reached. At the initial time t_i, we set the radius to $R_i = 1$, the expansion rate in the linear regime during matter domination to $\mathrm{d}R/\mathrm{d}t|_i = 2\left(1 - \delta_{\mathrm{m},i}/3\right)/(3t_i)$, and employ equation (7) for the initial dark energy density contrast.

We checked that solving for the radius of the spherical overdensity using equations (8) and (9) gives the same time of collapse as obtained from the non-linear set of equations (3)-(5). In fact, these two approaches are equivalent. This can for example be shown for dynamical mutation of dark energy, as in Abramo et al. (2008). Here, for the collapse overdensity we have $p_{\mathrm{c}} = w_{\mathrm{c}}\rho_{\mathrm{c}}$ and $\rho_{\mathrm{c}} = \bar{\rho}(1+\delta)$, for which the continuity equation (9) reads $\dot{\delta} + 3(1+\delta)[h(1+w_{\mathrm{c}}) - H(1+w)]$, with $h = \dot{R}/R$. This is the

same as equation (3) when expressing the equation of state inside the overdensity, w_c, in terms of the background equation of state via $w_c = w + (c_s^2 - w)\,\delta/(1+\delta)$. We additionally include the approach of following the radius evolution, as we directly connect the radii at turn-around with the radii at virialisation through energy conservation. This will be needed in Sections 2.3 and 2.4.

Note that for dark energy sound speeds different from one or zero the top-hat profile evolution for density perturbations, with which equations (3)-(5) comply, does not hold. The absence of a sharp top-hat profile leads to a scale- (or mass-) dependence in the perturbations, which propagates to derived quantities like the density threshold of collapse, so that either an interpolation down to the well-behaved case of sound speed zero or an averaging of the derived quantities, e.g. the threshold of collapse, over a top-hat profile are necessary (Basse et al. 2011; Basse et al. 2014). We can define a Jeans mass depending on the sound speed of the dark energy fluid. This leads to a characteristic scale, where the effects of clustering due to dark energy perturbations becomes important. For example, sound speeds of the order of 10^{-4} and 10^{-5} correspond to masses of the order of $10^{14} M_\odot$ and $10^{15} M_\odot$, respectively, which are typical masses for galaxy clusters. In this work we opt for comparing cold dark energy of negligible sound speed against the standard quasi-homogeneous dark energy. The advantage is that these two limiting cases are fully consistent with the semi-analytical treatment described above, in which the top-hat evolution of the spherical overdensity is physically motivated.

2.2 Collapse threshold

Here we discuss the cosmology-dependent linear density threshold of collapse for exemplary parameter values of the present-day matter density and dark energy equation of state. To solve for the evolution of a spherical overdensity we evolve equations (3)-(5) until the non-linear density perturbation diverges and the point of collapse is reached. The linear density contrast of matter at the time of collapse is the so-called spherical collapse threshold δ_c. In an Einstein-de Sitter (EdS) universe (i.e. $\Omega_m = 1$) $\delta_c = 1.686$, independent of redshift and initial overdensity (see e.g. Bertschinger & Jain 1994; Martel & Shapiro 1999). The inclusion of dark energy modifies the dynamics of the spherical collapse, introducing a redshift-dependence in the threshold of collapse. This redshift dependency of the collapse threshold is displayed in the top left panel of Fig. 1 for a $w \in [-1.4, -0.6]$ in steps of 0.2 from top to bottom, for $c_s^2 = 1$ and $c_s^2 = 0$. Note that for ΛCDM, i.e. $w = -1$, these two cases coincide. The presence of non-phantom dark energy with $w > -1$ lowers δ_c with respect to that of ΛCDM, while dark energy with $w < -1$ has the opposite effect. For cold dark energy, instead, the collapse threshold is lowered for $w < -1$ and enhanced for $w > -1$.

As can be seen from the radius evolution of the spherical overdensity in the middle panels of Fig. 1, the change of collapse dynamics with w translates into a slightly delayed collapse in a cold dark energy scenario as opposed to quasi-homogeneous dark energy for $w < -1$. This is because dark energy becomes important earlier, hindering the collapse. The opposite is true for $w > -1$, where spherical overdensities collapse earlier, as dark energy starts to dominate later. In all cases, cold dark energy tends to bring radius evolution and collapse threshold closer to those of ΛCDM. Also, the modification of the spherical collapse dynamics by the inclusion of dark energy becomes more apparent when further away from an EdS scenario, i.e. the lower Ω_m the lower δ_c. This behaviour is shown in the top right panel of Fig. 1 for different values of $\Omega_m < 1$, with $w = -1$ fixed.

2.3 Virial overdensity

In the context of the Press-Schechter formalism (Press & Schechter 1974) and its extensions (see e.g. Zentner 2007), a halo mass is defined as the mass enclosed by the virial radius R_{vir} within which there is an interior mean overdensity Δ_{vir} with respect to a reference background density $\bar{\rho}_{ref}$. In general, the virial overdensity Δ_{vir} depends on redshift and cosmology. On the other hand, observational masses are associated with more convenient fixed overdensities, with typical values such that the interior average density is $\rho_{int} = 300\bar{\rho}_m$ or $\rho_{int} = 500\bar{\rho}_{crit}$, where $\rho_{crit} = 3H_0^2/(8\pi G)$ is the critical density of the Universe. Thus, to compare the predicted number of collapsed objects with cluster number count data we need to derive Δ_{vir} explicitly for each cosmology.

In the spherical collapse framework the time, or redshift, of virialisation is obtained by relating it to the turn-around of the collapsing sphere via the virial theorem. The time of turn-around is reached when the radius of the sphere is maximal, and equivalently the quantity $\log(\delta_{NL}+1)/a^3$, with non-linear density contrast δ_{NL}, is minimal (Pace et al. 2010) before diverging at the time of collapse. Radius and overdensity at turn-around can then be connected to radius and overdensity at virialisation by making use of energy conservation. We use the connection between virial and turn-around radius as given in Lahav et al. (1991), where the virial radius gives us the time, or scale factor, of virialisation by tracking the radius evolution of the sphere as described in Section 2, in equations (8) and (9). Having the time and radius of virialisation, the virial overdensity Δ_{vir} is due to mass conservation given by (Basilakos et al. 2009; Lee & Ng 2010; Meyer et al. 2012)

$$\Delta_{vir} = (\delta_{NL,vir}+1) = (\delta_{ta}+1)\left(\frac{a_{vir}}{a_{ta}}\right)^3\left(\frac{R_{ta}}{R_{vir}}\right)^3, \tag{10}$$

where a_{ta} and R_{ta} are the turn-around scale factor and radius, and a_{vir} and $\delta_{NL,vir}$ are the scale factor and non-linear density contrast, respectively, at the time of virialisation.

The virial overdensity needs to be calculated for every redshift and cosmological parameter set of interest. In order to speed up the calculations, we fit the virial density threshold on a grid of both Ω_m and w, aiming at sub-percent accuracy. The fitting formula is an expansion around the EdS case at $\Omega_m = 1$ of constant $\Delta_{vir} = 18\pi^2$. It reads

$$\Delta_{vir}(z) = \frac{\left[18\pi^2 + a(1-\Omega_m(z)) + b(1-\Omega_m(z))^2\right]}{\Omega_m(z)}, \tag{11}$$

with fitting parameters a, b, and the fractional matter density parameter $\Omega_m(z)$. For our halo mass function calculations in Section 3, we interpolate the values of the virial density threshold on the fitted grid to convert observed cluster masses to virial masses.

The bottom panels of Fig. 1 show the virial overdensity

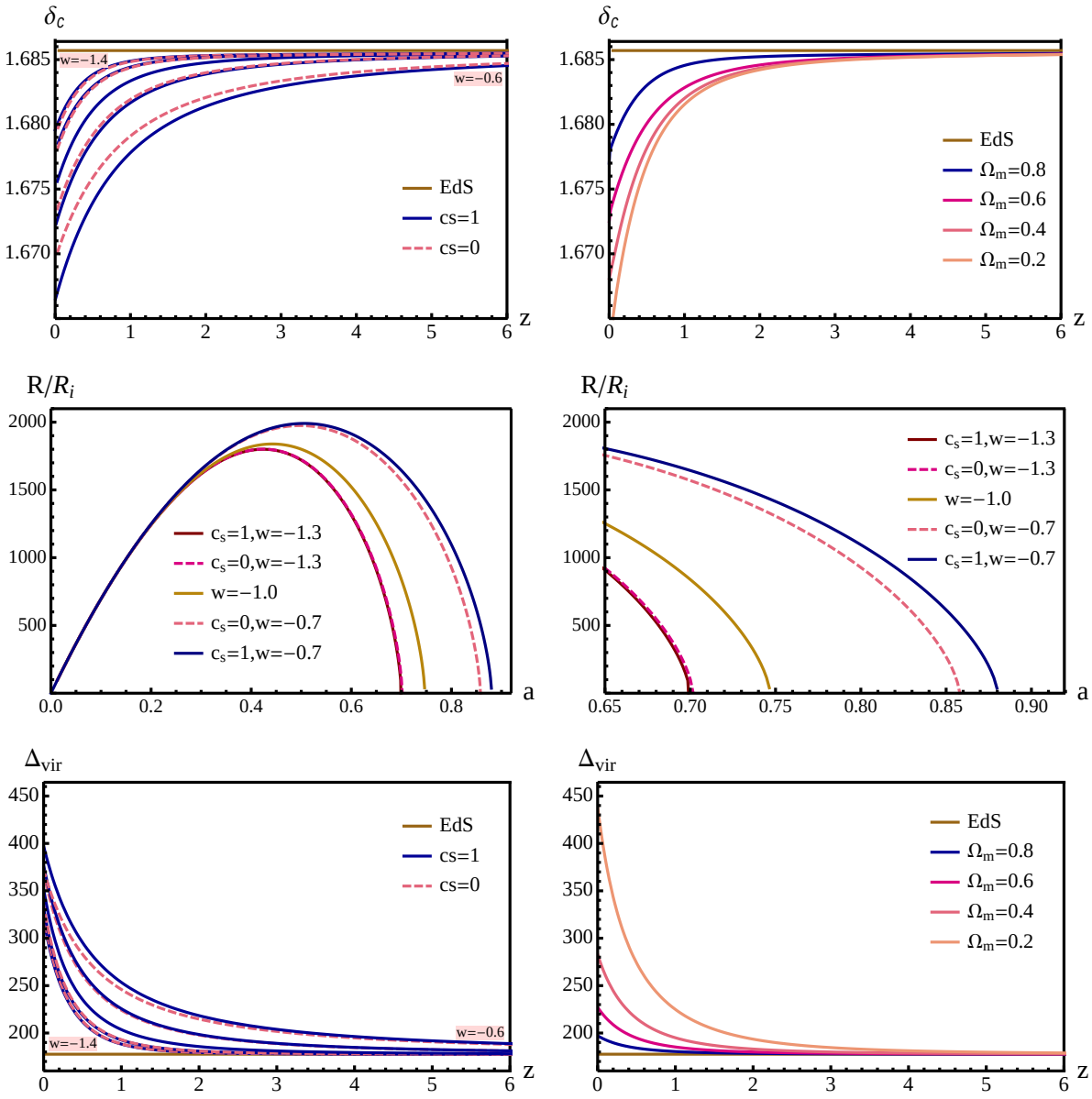

Figure 1. Top left panel: Collapse threshold δ_c as a function of redshift for $w=-1.4$ to $w=-0.6$ in steps of 0.2 (top to bottom curves) for fixed $\Omega_m=0.3$. Solid blue curves correspond to cases of quasi-homogeneous dark energy with sound speed $c_s=1$, and dashed magenta curves of cold dark energy with sound speed $c_s=0$. The EdS case with constant $\delta_c=1.686$ is shown in brown. Top right panel: $\delta_c(z)$ for fixed $w=-1$ and curves of varying Ω_m as indicated. Middle left panel: Time evolution of the radius R over the initial radius R_i of spherical overdensities for $w=-1.3,-1,-0.7$, and fixed $\Omega_m=0.3$, for $c_s=1$ (solid curves) and $c_s=0$ (dashed curves). Middle right panel: Detail of the middle left panel. Bottom left panel: Virial overdensity Δ_{vir} as a function of redshift for $c_s=1$ (solid) and $c_s=0$ (dashed) with w varying as indicated from $w=-1.4$ to $w=-0.6$ in steps of 0.2 (top to bottom curves), and fixed $\Omega_m=0.3$. The EdS value of $\Delta_{vir,EdS}=18\pi^2$ is shown in brown. Bottom right panel: $\Delta_{vir}(z)$ for Ω_m as indicated, and $w=-1$ fixed. Note that for $w=-1$ all these quantities are the same for the two speeds of sound.

for different values of w and Ω_m. As it was the case in Section 2.2 for the collapse threshold, the presence of dark energy tends to increase the virial density threshold compared to the constant EdS case. The effect is bigger the earlier dark energy becomes important. When comparing cold to quasi-homogeneous dark energy in the bottom left panel of Fig. 1, the virial overdensity is larger for $w<-1$, as collapse is hindered, and lower for $w>-1$, with cold dark energy helping the collapse in this case. For a cosmological constant, the bottom right panel of Fig. 1 makes clear again that lowering Ω_m increases the virial overdensity.

2.4 Dark energy mass contribution

In the case of cold dark energy, where dark energy of negligible sound speed is comoving with dark matter, dark energy perturbations can contribute to the total mass of the object. We therefore include the contributions from dark energy perturbations to the total mass by altering the predicted halo

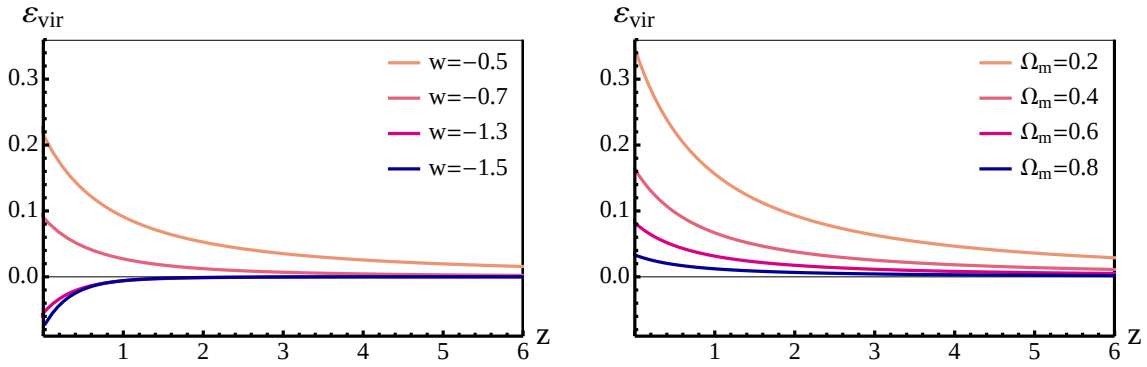

Figure 2. Left panel: Ratio $\varepsilon_{\rm vir}$ between the dark energy mass $M_{\rm vir,de}$ and cold dark matter mass $M_{\rm vir,m}$ at virialisation as a function of redshift. Ω_m is fixed to 0.3 and w varies as indicated. Right panel: The same quantity $\varepsilon_{\rm vir}(z)$ for w fixed to -0.5 and Ω_m varying as indicated.

mass function. To estimate the extra dark energy contribution to the total mass, we calculate the dark energy mass at virialisation as shown in Creminelli et al. (2010a). We assume a top-hat profile and calculate the virial radius $R_{\rm vir}$ as in Section 2.3 within the spherical collapse framework. We define the dark energy mass contribution at virialisation as

$$M_{\rm vir,de} = 4\pi \int_0^{R_{\rm vir}} {\rm d}R R^2 \delta_{\rm de}\,, \tag{12}$$

with non-linear dark energy density contrast $\delta_{\rm de}$. The total halo mass M is then rescaled by the dark energy mass contribution as $M \to M\left(1+M_{\rm vir,de}/M_{\rm vir,m}\right)$. This ratio between dark energy and dark matter mass at virialisation $\varepsilon_{\rm vir}(z) = M_{\rm vir,de}/M_{\rm vir,m}$ is shown in the left panel of Fig. 2 for different values of w. As expected, the extra dark energy mass contribution grows further as w deviates from the ΛCDM value of $w=-1$, i.e. with increasing inhomogeneity, and changes sign from a positive to a negative contribution when going from the non-phantom $w>-1$ to the phantom $w<-1$ side. The right panel of Fig. 2 shows the ratio $\varepsilon_{\rm vir}(z)$ for different values of $\Omega_{\rm m}$ and fixed $w=-0.5$. The positive mass correction is higher the lower $\Omega_{\rm m}$, as the dark energy mass contribution increases compared to that of dark matter. Generally, the dark energy contribution also becomes more significant at lower redshifts for the same reason.

An alternative to integrating only over the perturbed dark energy density $\delta_{\rm de}$ is to include also the dark energy background density in equation (12), which leads to slightly higher deviations. The inclusion of this smooth background dark energy component in the calculation of mass is debatable though. Another possibility is to rescale the total mass by integrating over a dark energy accretion rate for the halo, see again Creminelli et al. (2010a). As a conservative, lower estimate, throughout this paper we will use only the dark energy mass contribution from the inhomogeneous part.

3 RE-CALIBRATED HALO MASS FUNCTION

In this section we show the impact of cold dark energy on the halo mass function (HMF), i.e. the comoving number density of halos as a function of mass and redshift. We also re-calibrate the standard HMF for cold dark matter to account for non-linear perturbative effects stemming from dark energy being cold (clustering) instead of quasi-homogeneous. To do so we include the non-linear characteristic quantities derived in Section 2 into our mass function re-calibration, as described below. For this, it is crucial to evaluate these quantities, i.e. $\delta_{\rm c}$, $\varepsilon_{\rm vir}$ and $M_{\rm vir,de}$, for each set of cosmological parameters when estimating and forecasting constraints in Section 5 and Section 6, respectively.

In practice, we calculate both the Tinker HMF (Tinker et al. 2008) and the Sheth-Tormen HMF (Sheth & Tormen 1999) for each set of cosmological parameters. We then form the ratio between the Sheth-Tormen HMF of cold dark energy to the Sheth-Tormen HMF of quasi-homogeneous dark energy and multiply it by the standard Tinker HMF. The ratio of Sheth-Tormen HMFs therefore encapsulates the difference between cold and quasi-homogeneous dark energy, i.e. the impact of cold dark energy on the halo mass function. The functional form of the Tinker HMF is based on linear perturbation theory and provides an accurate (enough) fit to cold dark matter N-body simulations. The re-calibrated HMF for the expected number of halos of mass M at redshift z in a cold dark energy scenario reads

$$\frac{{\rm d}n_{\rm cal}}{{\rm d}M}(M,z) = \frac{{\rm d}n_{\rm ST}/{\rm d}M\,(M,z;c_{\rm s}=0)}{{\rm d}n_{\rm ST}/{\rm d}M\,(M,z;c_{\rm s}=1)} \times \frac{{\rm d}n_{\rm T}}{{\rm d}M}(M,z)\,, \tag{13}$$

with "ST" designating a Sheth-Tormen and "T" a Tinker HMF. A similar ratio has been employed in Sartoris et al. (2010b) and Cataneo et al. (2015) in order to constrain primordial non-Gaussianity, as first prescribed in LoVerde et al. (2008), in the former, and to distinguish $f(R)$ modified gravity theories from GR+ΛCDM, in the latter.

As a reminder, the Tinker HMF is defined by the multiplicity function $f(\sigma)$ (Tinker et al. 2008)

$$f(\sigma) = A\left[\left(\frac{\sigma}{b}\right)^{-a}+1\right]e^{-c/\sigma^2}\,, \tag{14}$$

with the parameters fitted using cold dark matter simulations, and the functional form of a HMF under spheroidal collapse

$$\frac{{\rm d}n_T}{{\rm d}M}(M,z) = f(\sigma)\frac{\bar{\rho}_{\rm m}}{M}\frac{{\rm d}\log\sigma^{-1}}{{\rm d}M}\,. \tag{15}$$

The parameters A, a, b and c depend on the definition of cluster mass as multiples of the overdensity Δ with respect to $\rho_{\rm crit}$. The variance $\sigma(R)$ of the density field smoothed at

radius R is defined as

$$\sigma^2(R) = \frac{1}{2\pi^2}\int P(k)\,|W(kR)|^2\,k^2 \mathrm{d}k\,. \tag{16}$$

This integrates the matter power spectrum $P(k)$ over the top-hat window function $W(kR)$ for a sphere of radius R in Fourier space. The theoretical uncertainty of the Tinker HMF from simulations is $\leq 5\%$. We include this uncertainty in our cluster analysis by increasing the width of the Gaussian priors on the parameters of the HMF to 10%, as well as accounting for their covariance.

The Sheth-Tormen HMF accounts for ellipsoidal instead of spherical collapse, giving an improved fit to numerical simulations. It is given by the multiplicity function (Sheth & Tormen 1999)

$$\nu f(\nu) = A\sqrt{\frac{2a\nu^2}{\pi}}\left[1+\left(a\nu^2\right)^{-p}\right]\exp\left[-a\nu^2\right], \tag{17}$$

with parameters a and p fitted to simulations, where a is determined by the number of massive halos, p by the shape of the mass function at the low mass end, and A is the normalization ensuring the integral of $f(\nu)$ over all ν gives unity. The functional form for the HMF states

$$\frac{\mathrm{d}n_{\mathrm{ST}}}{\mathrm{d}M}(M,z) = \nu f(\nu)\frac{\bar{\rho}_{\mathrm{m}}}{M^2}\frac{\mathrm{d}\log\nu}{\mathrm{d}\log M}\,. \tag{18}$$

$f(\nu)$ depends now on the peak height $\nu = \delta_{\mathrm{c}}/\sigma$, with collapse threshold $\delta_{\mathrm{c}}(z)$, and not solely on σ as in the case of the Tinker HMF. As can be seen in equation (18), the Sheth-Tormen HMF depends on the cosmological background via the mean matter density $\bar{\rho}_m$, as well as on linear density perturbations through σ and the linear growth function $D(z)$.

When comparing the halo mass function to observations, the non-linear information on the properties of collapsed structures can be included via δ_{c}, Δ_{vir} and $\varepsilon_{\mathrm{vir}}$. Generally, these quantities are redshift-dependent, as well as change with cosmology, and therefore depend on the dark energy sound speed. Comparing structure formation data to theoretical expectations, collapse threshold and virial overdensity sometimes are taken at their constant EdS values, or as fitting functions for a ΛCDM cosmology (see e.g. Kitayama & Suto (1996) and Nakamura & Suto (1997)).

We go beyond this practice and advocate a more accurate calibration of the model-dependent non-linearities in the halo mass function by using the results obtained within the spherical collapse framework shown in Sections 2.2 to 2.4. We then insert $\delta_{\mathrm{c}}(z)$ for a given cosmology into the Sheth-Tormen HMF of equation (18), both for quasi-homogeneous and cold dark energy, and form the ratio in equation (13). We convert between observed cluster and virial masses, defined using Δ_{vir} from Section 2.3, assuming a Navarro-Frenk-White (NFW) profile (Navarro et al. 1996; Hu & Kravtsov 2003). The standard use of the NFW profile comes from N-body simulations with a quasi-homogeneous dark energy component only in a background and cold dark matter particles. However, we expect this profile to hold reasonably well for a case with cold dark energy, since for negligible sound speed dark energy is comoving with dark matter and therefore should not significantly alter the radial profile. We also include the mass correction at virialisation due to dark energy calculated as in Section 2.4. This accounts for differences in virialisation, as well as for the mass shift introduced in the halo mass function due to cold dark energy.

In the top left panel of Fig. 3 we show the re-calibrated mass function of equation (13) as a function of virial mass for both $c_{\mathrm{s}} = 1$ and $c_{\mathrm{s}} = 0$, and $w = -1$ (ΛCDM), $w < -1$ and $w > -1$, with $\Omega_{\mathrm{m}} = 0.3$ fixed for all curves. The predicted cluster abundances are systematically lower for cold compared to quasi-homogeneous dark energy when $w < -1$, and systematically higher for $w > -1$. For $w = -1$ both curves coincide, as dark energy perturbations vanish. This behaviour is to be expected, since the contribution from dark energy perturbations suppresses structure formation for $w < -1$ and enhances it for $w > -1$ with respect to the quasi-homogeneous case. The bottom left panel of Fig. 3 underlines these sizeable deviations, showing the ratio between the Sheth-Tormen cluster mass functions of $c_{\mathrm{s}} = 0$ to $c_{\mathrm{s}} = 1$ dark energy for different values of w. We re-calibrate the halo mass function with this ratio. The top right panel of Fig. 3 shows the ratio between the re-calibrated cluster mass functions for cold and quasi-homogeneous dark energy to the mass function in a ΛCDM universe for the same set of parameters as in the top left panel. For a cold dark energy scenario, this ratio indicates deviations from ΛCDM by up to a number of times, depending on the mass and parameters chosen. The effect is especially pronounced at the high-mass end where massive clusters of galaxies reside. The bottom right panel of Fig. 3 shows the dependence on Ω_{m} of the re-calibrated cluster mass function, for both $c_{\mathrm{s}} = 1$ and $c_{\mathrm{s}} = 0$ dark energy. We display curves for $\Omega_{\mathrm{m}} = 0.2, 0.3, 0.4$ at fixed $w = -0.7$. As expected, the predicted cluster abundances are systematically higher for cold compared to quasi-homogeneous dark energy as it was in the corresponding case in the bottom left panel for a $w > -1$. Note that the difference between cold and quasi-homogeneous dark energy is more pronounced for low matter densities, as the relative importance of dark energy grows.

Even though here we focused on displaying the parameter dependence of the mass function re-calibration on Ω_{m}, w and c_{s}, we want to stress that the mass function estimate to be obtained with our Markov Chain Monte Carlo (MCMC) data analysis crucially depends on a multitude of parameters, such as those of the mass-observable relations fitted simultaneously with cosmology. In Section 5 we will use the re-calibrated mass functions presented here to constrain cosmological parameters with measurements of cluster number counts.

4 DATA

For the parameter constraints in Section 5 we present results from both a cluster-only data set and a combination of clusters, CMB, baryon acoustic oscillation (BAO), and type Ia supernova (SN Ia) data. The cluster data used here[1] consist of three X-ray samples of clusters taken from the ROSAT All-Sky Survey (RASS; Truemper 1993), the Brightest Cluster Sample (BCS; Ebeling et al. 1998), the ROSAT-ESO Flux Limited X-ray sample (REFLEX; Boehringer et al.

[1] Note that we do not include measurements of the gas mass fraction, f_{gas}, experiment (Mantz et al. 2014), as the relation between X-ray gas mass, total cluster mass and baryonic fraction has not been investigated yet for cold dark energy cosmology.

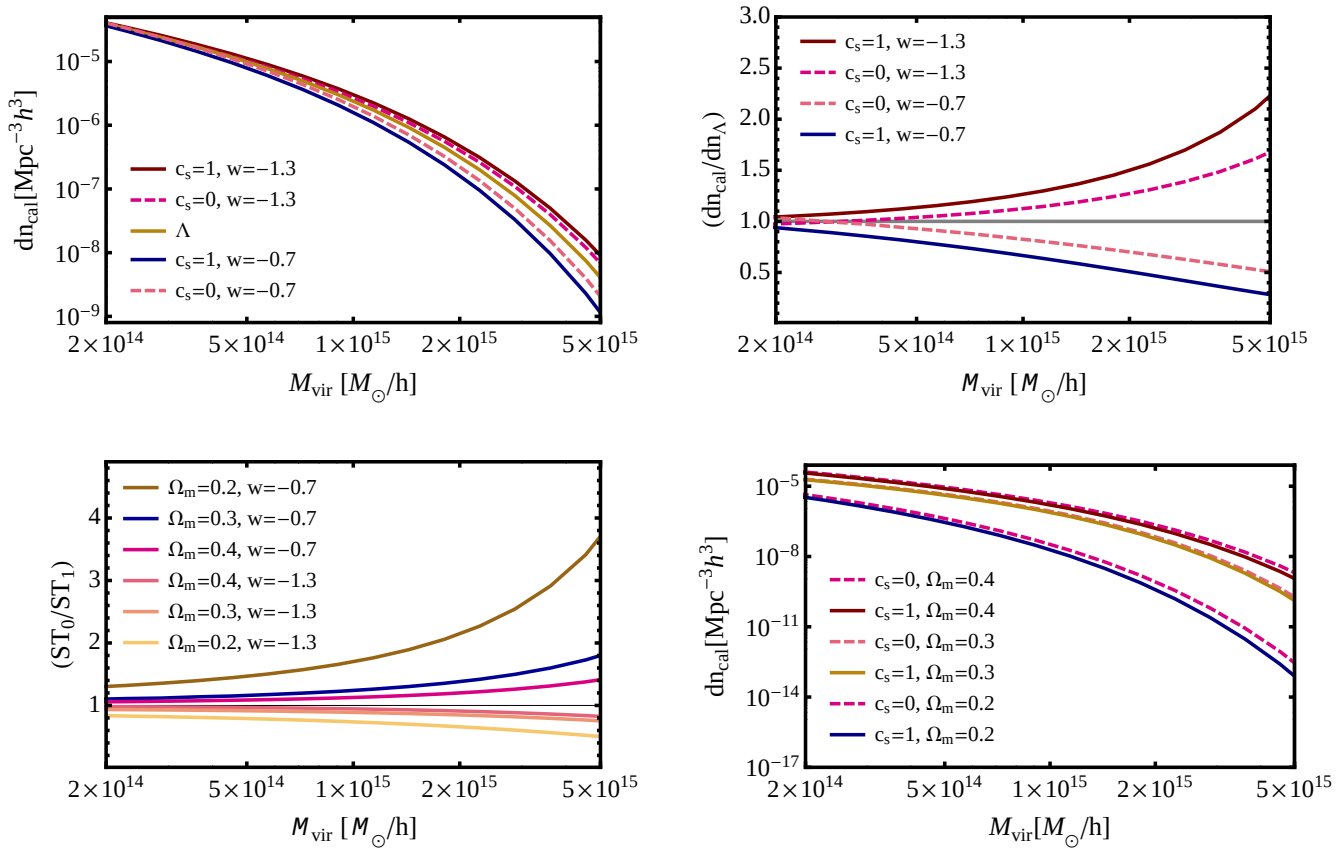

Figure 3. Top left panel: Re-calibrated halo mass functions at $z = 0$ for quasi-homogeneous dark energy ($c_s = 1$; solid lines) and cold dark energy ($c_s = 0$; dashed lines) for $w = -0.7$ (bottom curves) and $w = -1.3$ (top curves), as well as $w = -1$ for which both cases coincide. Ω_m is fixed to 0.3 for all curves. Top right panel: Ratios of re-calibrated halo mass functions with respect to the ΛCDM case at $z = 0$, for $c_s = 0$ (dashed) and $c_s = 1$ (solid). The ratios > 1 are for $w = -1.3$ and those < 1 for $w = -0.7$; this is the same in the next panel. Bottom left panel: Ratios of Sheth-Tormen HMFs for $c_s = 0$ over $c_s = 1$ dark energy at $z = 0$ for Ω_m values as indicated from the top to the bottom lines. Bottom right panel: Re-calibrated halo mass functions at $z = 0$ for $c_s = 1$ (solid) and $c_s = 0$ (dashed), and for $\Omega_m = 0.2, 0.3, 0.4$ bottom to top, with $w = -0.7$ fixed.

2004) and the bright sample of the Massive Cluster Survey (MACS; Ebeling et al. 2010), together with follow-up X-ray and optical imaging data. To select for high-mass clusters and avoid incompleteness, a flux limit of 0.1–2.4 keV luminosities $> 2.5 \times 10^{44} h^{-2}$ erg s^{-1} was applied; furthermore systems with X-ray emission dominated by active galactic nuclei have been removed. After cuts, the sample contains 224 clusters. For 94 clusters of the sample, follow-up ROSAT and/or *Chandra* data were used to derive X-ray luminosities and gas masses in order to constrain cluster scaling relations (see Mantz et al. 2010b). The absolute cluster mass scale is calibrated using state-of-the-art weak lensing measurements for 50 massive clusters taken from the Weighing the Giants program introduced in von der Linden et al. (2014), Applegate et al. (2014) and Kelly et al. (2014).

When using our cluster data set alone, consisting of RASS catalogues, and follow-up X-ray and lensing data, we also include Gaussian priors on the cosmic baryon density $100\,\Omega_b h^2 = 2.202 \pm 0.045$ (Cooke et al. 2014) and the present-day Hubble parameter $h = 0.738 \pm 0.024$ (Riess et al. 2011). For the full combination of clusters+CMB+BAO+SNIa, priors on h and Ω_b are not required. For the CMB data, we combine *Planck* (1-year release plus WMAP polarisation data; Planck Collaboration et al. 2014) together with Atacama Cosmology Telescope (ACT; Das et al. 2014) and South Pole Telescope (SPT; Keisler et al. 2011; Reichardt et al. 2012; Story et al. 2013) measurements at high multipoles. We also use the Union2.1 compilation of SNIa data (Suzuki et al. 2012), as well as BAO data from the 6-degree Field galaxy Survey (6dF; Beutler et al. 2011) and the Sloan Digital Sky Survey (SDSS; Padmanabhan et al. 2012; Anderson et al. 2014).

In the following we will employ both our cluster-only data set and its combination with the above complementary data sets to constrain cosmological parameters for both cold and quasi-homogeneous dark energy, using the re-calibrated mass function introduced in the previous section.

5 PARAMETER ESTIMATION

Here we present the first observational constraints on a dark energy model with constant w and $c_s = 0$. For this, we employ our cluster growth data both with and without additional complementary data sets, as described in the previous section.

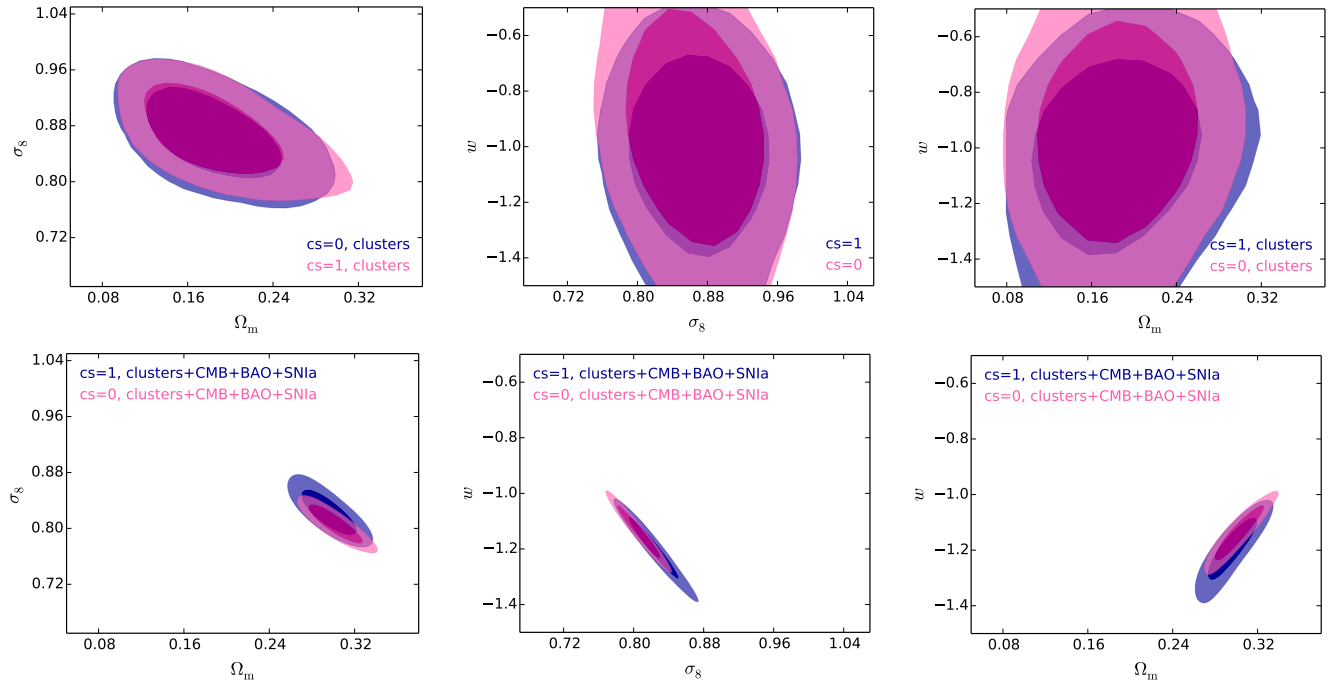

Figure 4. Confidence contours for quasi-homogeneous dark energy of sound speed $c_s = 1$ using a Tinker HMF (in blue), and for cold dark energy of sound speed $c_s = 0$ employing a re-calibrated mass function (magenta), using either cluster growth data only (upper panels) or a combination of these with CMB, BAO and SN Ia data as described in Section 4 (lower panels). Dark and light shading indicate the 68.3 and 95.4 per cent confidence regions.

Analysis	σ_8	Ω_m	w
Clusters only, $c_s = 0$	0.866 ± 0.039	0.186 ± 0.038	-0.96 ± 0.21
Clusters only, $c_s = 1$	0.870 ± 0.038	0.187 ± 0.041	-1.02 ± 0.18
Clusters + CMB + BAO + SNIa, $c_s = 0$	0.806 ± 0.014	0.302 ± 0.013	-1.14 ± 0.05
Clusters + CMB + BAO + SNIa, $c_s = 1$	0.823 ± 0.017	0.296 ± 0.013	-1.19 ± 0.07

Table 1. Marginalised best-fitting values and 68.3 per cent confidence intervals for σ_8, Ω_m and w, for both cold dark energy with sound speed $c_s = 0$ and quasi-homogeneous dark energy with $c_s = 1$. Results are shown for clusters-only and clusters+CMB+BAO+SNIa data as described in Section 4.

Our likelihood analysis and parameter estimation via an MCMC sampler includes theoretical and experimental scatter in the halo mass function and the mass-observable scaling relations, and also incorporates modified characteristic quantities for structure formation: collapse threshold (see Section 2.2), virial overdensity (Section 2.3) and cold dark energy mass contribution at virialisation (Section 2.4). These quantities are interpolated on a grid for computational speed, aiming at per cent accuracy. We proceed as follows. For each trial cosmology, the ratio of the Sheth-Tormen HMF for cold to that of quasi-homogeneous dark energy of equation (13) is formed, depending both on mass and redshift. Hereby the cosmology-dependent collapse threshold is included into the Sheth-Tormen HMF, on top of the background and linear level calculations taken from CAMB[2] (Lewis et al. 2000; Howlett et al. 2012). In addition, the cold dark energy mass contribution is taken into account, resulting in a shift of the mass scale, i.e. adding mass for $w > -1$ and reducing mass for $w < -1$ (see Section 2.4). Halo masses are then converted to virial masses assuming an NFW profile to map into any overdensity (Hu & Kravtsov 2003). Equation (13) is then used as our re-calibrated cold dark matter plus cold dark energy mass function to compare with observed cluster number counts. Virial masses are converted to observed masses using Δ_{vir}, as derived in Section 2.3, which accounts for differences in virialisation between the cold and quasi-homogeneous dark energy models.

We use a modified version of CosmoMC[3] (Lewis & Bridle 2002; Lewis 2013), which incorporates a module that evaluates our cluster growth likelihood (Mantz et al. 2015) using the data described in Section 4. We also employ uniform priors on $\Omega_m h^2 \in [0.025, 0.3]$, $\Omega_b h^2 \in [0.005, 0.1]$ and

[2] Version March 2013; http://camb.info/

[3] Version October 2013; http://cosmologist.info/cosmomc/

$w \in [-1.5, -0.5]$ in order to keep the spherical collapse calculations valid and numerically stable. Throughout our analysis, we assume a spatially flat cosmology, the standard effective number of relativistic species $N_{\rm eff} = 3.046$ and the minimal species-summed neutrino mass $\sum m_\nu = 0.056$.

Fig. 4 shows our constraints on $\Omega_{\rm m}$, w and the matter density field variance at 8 h^{-1}Mpc, σ_8, when using cluster growth data only (top panels), and the combination of cluster growth data with CMB, BAO and SN Ia data described in Section 4 (bottom panels). The blue contours show the results for the standard mass function analysis of quasi-homogeneous dark energy with sound speed $c_{\rm s} = 1$, employing the Tinker HMF, and the magenta contours those for cold dark energy with sound speed $c_{\rm s} = 0$. For the latter, we employ the re-calibrated cluster mass function of Section 3 as implemented into our cluster growth likelihood analysis. We find that the impact of assuming cold instead of quasi-homogeneous dark energy on these parameters is only marginal for current cluster data. For the combination of data sets, the slight shift between the confidence contours for cold versus quasi-homogeneous dark energy hints at an effect that will be important to investigate with upcoming, more precise measurements.

In Table 1 we show the corresponding marginalised best-fitting values and 68.3 per cent confidence intervals for σ_8, $\Omega_{\rm m}$ and w. The derived best-fitting values for cold and quasi-homogeneous dark energy agree within their respective 68.3 per cent confidence intervals for cluster growth data only. Both cases display a slight preference for phantom ($w < -1$) values of the dark energy equation of state, and their confidence intervals are similar in size for current data. For the full combination of clusters+CMB+BAO+SNIa data though, differences in the marginalised best-fit values at the 1–2 σ-level start to appear between cold and quasi-homogeneous dark energy, as to be expected, already for present-day data. This indicates that interesting avenues might be opening up in the future with improved data. Another example would also be the ability to constrain the dark energy sound speed using structure formation data in the non-linear regime sensitive to scale-dependent behaviour, which occurs for sound speeds different from zero or one.

6 FISHER FORECAST

In this Section we use a Fisher matrix formalism to forecasts constraints on cosmological parameters from cluster number counts for the case of both cold and quasi-homogeneous dark energy. We want to address the question of whether the choice between these two models will have a significant impact on the inference of parameters such as w for upcoming cluster constraints. For this analysis we use the cosmological parameter vector $\mathbf{p} = \{\Omega_{\rm m}, \Omega_{\rm b}, h, n_{\rm s}, \sigma_8, w\}$, of which we only vary three of them: $\Omega_{\rm m}$, σ_8 and w. As fiducial values we take those of the Planck best-fit for the base case wCDM lowl+highL+SNLS in Planck Collaboration et al. (2014)[4,5], being $\Omega_{\rm m} = 0.28$, $\Omega_{\rm b} = 0.044$, $h = 0.709$, $n_{\rm s} = 0.9581$, $\sigma_8 = 0.87$ and $w = -1.124$. Note also that we do not include a galaxy cluster power spectrum analysis.

The Fisher matrix for cluster number counts, with $N_{l,m}$ number of clusters in the l-th redshift bin and m-th observed mass bin, reads (Holder et al. 2001)

$$F_{ij} = \sum_{l,m} = \frac{\partial N_{l,m}}{\partial p_i} \frac{1}{N_{l,m}} \frac{\partial N_{l,m}}{\partial p_j}, \tag{19}$$

where the inverse covariance is given by $C^{-1}_{l,m} = 1/N_{l,m}$. The $N_{l,m}$ expected for a survey with sky coverage $\Delta\Omega$ is (Majumdar & Mohr 2003)

$$N_{l,m} = \frac{\Delta\Omega}{4\pi} \int_{z_l}^{z_{l+1}} {\rm d}z \frac{{\rm d}V}{{\rm d}z} \int_{M^{\rm ob}_{l,m}}^{M^{\rm ob}_{l,m+1}} \frac{{\rm d}M^{\rm ob}}{M^{\rm ob}} \int_0^{+\infty} {\rm d}M\, n(M,z)\, p\left(M^{\rm ob}|M;z\right), \tag{20}$$

with comoving volume element per unit redshift interval ${\rm d}V/{\rm d}z$, halo mass function $n(M,z)$, and probability to assign an observed mass $M^{\rm ob}$ to a cluster of true mass M, $p\left(M^{\rm ob}|M\right)$. The cosmology-dependent comoving volume element is given by

$$\frac{{\rm d}V}{{\rm d}z} = \frac{4\pi c\,(1+z)^2}{H(z)} d_{\rm A}^2(z), \tag{21}$$

with angular diameter distance $d_{\rm A}(z)$ and Hubble function $H(z)$. For quasi-homogeneous dark energy with sound speed $c_{\rm s} = 1$ we use the halo mass function $n(M,z)$ from Tinker et al. (2008) at an overdensity of $\Delta = 200$ with respect to the background density. For cold dark energy with sound speed $c_{\rm s} = 0$, we use instead the re-calibrated HMF of equation (13) with cosmology-dependent $\delta_{\rm c}$ (Section 2.2) and $\varepsilon_{\rm vir}$ (Section 2.4). It is worth noting that here $\varepsilon_{\rm vir}$ effectively introduces a mass bias between true and observed mass.

Following Lima & Hu (2005) and assuming a lognormal distribution with variance $\sigma^2_{\ln M}$ we have

$$p\left(M^{\rm ob}|M;z\right) = \frac{\exp\left[-x^2\left(M^{\rm ob},M,z\right)\right]}{\sqrt{\left(2\sigma^2_{\ln M}(z)\right)}}, \tag{22}$$

where $x\left(M^{\rm ob},M,z\right)$ relates true and observed mass as

$$x\left(M^{\rm ob},M,z\right) = \frac{\ln M^{\rm ob} - \ln M_{\rm bias}(z) - \ln M}{\sqrt{\left(2\sigma^2_{\ln M}(z)\right)}}. \tag{23}$$

And inserting equation (22) into equation (20) we have,

$$N_{l,m} = \frac{\Delta\Omega}{4\pi} \int_{z_l}^{z_{l+1}} {\rm d}z \frac{{\rm d}V}{{\rm d}z} \int_0^{+\infty} {\rm d}M\, n(M,z) \left[{\rm erfc}\,(x_m) - {\rm erfc}\,(x_{m+1})\right], \tag{24}$$

with $x_m = x\left(M^{\rm ob}_{l,m}, M, z_l\right)$.

As in Sartoris et al. (2010b); Sartoris et al. (2016), we model the mass-observable relation using the bias between observed and true masses $\ln M_{\rm bias}$ and the intrinsic scatter $\sigma^2_{\ln M}$ as

$$\ln M_{\rm bias}(z) = B_{\rm M,0} + \alpha \ln(1+z),$$
$$\sigma^2_{\ln M}(z) = \sigma^2_{\ln M,0} - 1 + (1+z)^{2\beta}, \tag{25}$$

with fiducial parameters

$$\mathbf{p_N} = \left\{B_{M,0} = 0,\, \alpha = 0,\, \sigma_{\ln M,0} = 0.4,\, \beta = 0.0\right\}. \tag{26}$$

[4] https://wiki.cosmos.esa.int/planckpla/index.php/Cosmological_Parameters
[5] PLA/base_w_planck_lowl_lowLike_highL_post_SNLS

Survey	$f_{\rm sky}[\%]$	$M_{\rm thr}$ $[M_\odot]$	$\Delta\log(M/M_\odot)$	$z_{\rm max}$	Δz
DES	12	1×10^{14}	0.2	1.0	0.05

Table 2. Survey specifications used to Fisher matrix forecast cosmological parameters with cluster number counts, see Section 6.

For the quasi-homogeneous dark energy model, this choice of fiducial parameters corresponds to no bias in the mass-observable scaling relation. For cold dark energy, the shift between true and observed mass introduced by $\epsilon_{\rm vir}$ translates into a mass- and redshift-dependent mass bias. Also, a mass scatter of $\sigma_{\ln M}=0.4$ is assumed. We selected the mass-observable scaling relation parameters to be consistent with the observed mass-richness relation for massive, X-ray selected clusters at z<0.5 (Mantz et al. 2016). The richness measurements for that relation were drawn from Sloan Digital Sky Survey (SDSS) data using the redMaPPer algorithm (Rykoff et al. 2014; Rozo et al. 2015), which is a red sequence cluster finder designed to handle an arbitrary photometric galaxy catalog with excellent photometric redshift performance, completeness and purity, and which is currently in use for Dark Energy Survey (DES) cluster studies. We caution, however, that the scatter chosen may be optimistic when applied to optically selected clusters, as in some cases projection effects can boost the measured richness. Also, the redshift evolution of the scatter is not well known and the details will depend on the selection algorithm used. We therefore assume that it remains constant. Even though the validity of this assumption may deteriorate at higher redshifts, because there the impact of projection effects is expected to increase.

We choose our fiducial nuisance parameters for the mass-observable scaling relation to be representative of those currently expected for DES[6]. In our Fisher matrix forecast we fix the nuisance parameters α, $\sigma_{\ln M,0}$ and β to their fiducial values and account for the expected uncertainty in the absolute mass calibration by leaving $B_{M,0}$ to vary within 3%. The cluster mass threshold of detection $M_{\rm thr}$ is approximated as independent of redshift, although in practice $M_{\rm thr}$ becomes higher at higher redshifts depending on the survey-specific selection function. For DES, we use a sky coverage of $5000\,{\rm deg}^2$ from $z=0.1$ out to $z=1.0$ with $\Delta z=0.05$ to match the expected photo-z error for masses larger than $M_{\rm thr}\approx10^{14}M_\odot$ (Abbott et al. 2016; Rykoff et al. 2016). We bin the mass in steps of $\Delta\log\left(M^{\rm ob}/M_\odot\right)=0.2$ from the threshold mass $M_{\rm thr}$ up to a maximum of $\log\left(M^{\rm ob}/M_\odot\right)\leq16$. The survey specifications used for the Fisher matrix forecasts performed in this section are summed up in Table 2. Fig. 5 shows the redshift-binned number density of clusters to be expected for DES in the redshift range $0.1<z<1.0$ for both cold (magenta) and quasi-homogeneous (blue) dark energy. The inset panel shows the corresponding ratio of $c_s=1$ over $c_s=0$, with about 3% more clusters detected in the $z=0.1-0.2$ bin in the $c_s=1$ model.

For this analysis, we have implemented our halo mass function re-calibration of Section 3 and the Fisher matrix

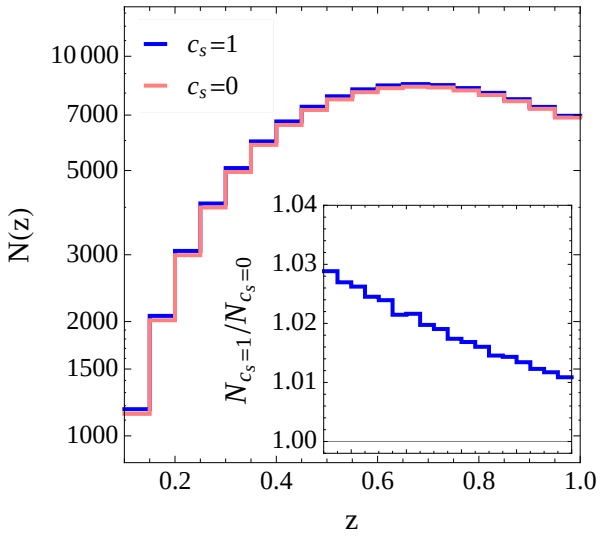

Figure 5. Number density of detected clusters for $c_s=1$ (blue line) and $c_s=0$ (magenta line), and the corresponding ratio of $c_s=1$ over $c_s=0$ (inset), for the survey characteristics of DES in Table 2, and for the fiducial cosmological and nuisance parameter values as stated in the text.

calculation for cluster number counts sketched above into the publicly available CosmoSIS code (Zuntz et al. 2015)[7]. Within the latter we ran the provided Fisher matrix sampler together with CAMB[8], making use of the existing routine[9] for the calculation of the Tinker and Sheth-Tormen HMFs.

In Fig. 6 we show the resulting marginalised forecasted constraints for cold (dashed, magenta contours) versus quasi-homogeneous (solid, blue contours) dark energy, where we find that those for cold dark energy are tighter. The differences in marginalised confidence intervals are summed up in Table 3, together with a Figure of Merit (FoM) that we define similarly to that of the Dark Energy Task Force (DETF – Albrecht et al. 2006). That is, the square root of the determinant of the inverse Fisher matrix, ${\rm FoM}=1/\sqrt{|F_i^{-1}|}$, in our case in the (Ω_m,w) plane. We obtain constraints of the order of $\approx10^{-3}$ for Ω_m and σ_8, and $\approx10^{-2}$ for w, as well as a FoM $\approx10^4$, with that of the cold dark energy case being about a factor of 1.5 higher.

We note, that for *Euclid*[10] and Large Synoptic Survey Telescope (LSST)[11] data, with higher sky coverages and a larger redshift range, constraints on cosmological parameters are at least an order of magnitude stronger. Since both LSST and *Euclid* extend to higher redshifts than DES, investigating the impact of cold dark energy with a varying dark energy equation of state should be particularly interesting. We therefore, and due to the uncertain mass-observable scaling, postpone such analyses for later studies.

[6] http://www.darkenergysurvey.org

[7] Version 1.4; https://bitbucket.org/joezuntz/cosmosis/wiki
[8] Version January 2015.
[9] http://www.mpa-garching.mpg.de/~komatsu/crl/
[10] http://www.euclid-ec.org
[11] https://www.lsst.org/lsst_home.shtml

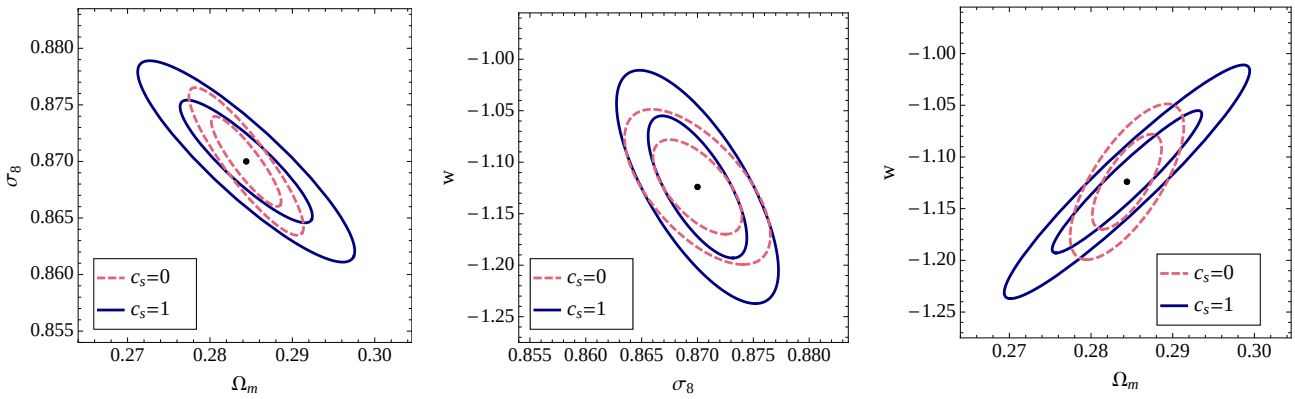

Figure 6. Forecasted constraints for DES as described in Section 6 for $c_s = 1$ (solid, blue contours) and $c_s = 0$ (dashed, magenta contours) at the 68.3 and 95.4 per cent confidence levels. Black dots mark the fiducial model of $\{\Omega_m, \sigma_8, w\} = \{0.287, 0.87, -1.124\}$.

	$\Delta\sigma_8$ $[10^{-3}]$	$\Delta\Omega_m$ $[10^{-3}]$	Δw $[10^{-3}]$	FoM $[10^3]$
$c_s = 0$	2.6	2.8	30.3	16.7
$c_s = 1$	3.2	5.6	45.5	10.8

Table 3. Marginalised 68.3 per cent confidence intervals for DES, for the Fisher matrix forecasts of Section 6 for both $c_s = 0$ and $c_s = 1$. We also show the FoM in the (Ω_m, w)-plane as defined in Section 6. The fiducial parameter values are $\{\Omega_m, \sigma_8, w\} = \{0.287, 0.87, -1.124\}$.

7 DISCUSSION

Cold dark energy of sound speed zero presents an interesting phenomenology by adding on top of the clustering of matter an extra clustering component due to dark energy perturbations that renders the model potentially distinguishable from standard quasi-homogeneous dark energy of sound speed one. Within the semi-analytical spherical collapse framework, in this paper we derived the non-linear characteristic quantities required for the re-calibration of the cluster mass function for cold dark energy. These are the collapse threshold, the virial overdensity and a dark energy mass contribution for cold dark energy. We incorporated these quantities into the halo mass function, including in this way the non-linear cosmological model information needed for a new cold dark matter plus cold dark energy mass function.

We used the re-calibrated mass function to constrain cosmological parameters for both quasi-homogeneous dark energy and cold dark energy with current state-of-the-art cluster growth data, as well as adding a combination of standard cosmological data sets. For the combined data set a shift in the best-fitting parameter values of up to one sigma can be detected, with for example $\sigma_8 = 0.806 \pm 0.014$ for sound speed zero and $\sigma_8 = 0.823 \pm 0.017$ for sound speed one. These results and the comparison of our re-calibrated mass functions for both models makes clear that including further non-linear model information has the potential to distinguish cold dark energy from the standard quasi-homogeneous case.

In order to predict the ability to distinguish cold versus quasi-homogeneous dark energy with upcoming cluster growth data, we Fisher matrix forecasted cosmological parameter constraints for ongoing and future surveys. We find that for the ongoing DES cluster survey, Ω_m and σ_8 constraints of the order of 10^{-3}, and of 10^{-2} for w, lead to a significant difference in our Figure of Merit, defined in the (Ω_m, w) plane, about 50% higher for cold dark energy. Besides these differences in the constraints, we also obtain differences in the directions of the parameter degeneracies between the cold and quasi-homogeneous dark energy models.

More and better data, as well as combinations with other data, should enhance the differences in the estimated parameters for cold versus quasi-homogeneous dark energy. An interesting direction for further studies would be a more realistic treatment that either allows both the dark energy sound speed and equation of state to vary as free parameters, or employs models for which these parameters naturally evolve with redshift.

ACKNOWLEDGEMENTS

The computational analysis was performed using the High Performance Computing facility at the University of Copenhagen (HPC@UCPH), and the Gardar supercomputer of the Nordic HPC project. DR is supported by a NASA Postdoctoral Program Senior Fellowship at the NASA Ames Research Center, administered by the Universities Space Research Association under contract with NASA. We acknowledge support from the U.S. Department of Energy under contract number DE-AC02-76SF00515, and from the National Aeronautics and Space Administration under Grant No. NNX15AE12G issued through the ROSES 2014 Astrophysics Data Analysis Program.

REFERENCES

Abbott T., et al., 2016, MNRAS, 460, 1270
Abramo L. R., Batista R. C., Liberato L., Rosenfeld R., 2008, Phys. Rev. D, 77, 067301
Abramo L. R., Batista R. C., Rosenfeld R., 2009, J. Cosmology Astropart. Phys., 7, 040

Albrecht A., et al., 2006
Allen S. W., Evrard A. E., Mantz A. B., 2011, ARA&A, 49, 409
Anderson L., et al., 2014, MNRAS, 439, 83
Appleby S. A., Linder E. V., Weller J., 2013, Phys. Rev., D88, 043526
Applegate D. E., et al., 2014, MNRAS, 439, 48
Applegate D. E., et al., 2016, MNRAS, 457, 1522
Armendariz-Picon C., Damour T., Mukhanov V. F., 1999, Phys. Lett., B458, 209
Armendariz-Picon C., Mukhanov V., Steinhardt P. J., 2000, Physical Review Letters, 85, 4438
Barreira A., Li B., Baugh C. M., Pascoli S., 2013, JCAP, 1311, 056
Basilakos S., Sanchez J. C. B., Perivolaropoulos L., 2009, Phys. Rev. D, 80, 043530
Basse T., Eggers Bjælde O., Wong Y. Y. Y., 2011, J. Cosmology Astropart. Phys., 10, 038
Basse T., Bjaelde O. E., Hamann J., Hannestad S., Wong Y. Y. Y., 2014, JCAP, 1405, 021
Batista R. C., Pace F., 2013, JCAP, 1306, 044
Bean R., Doré O., 2004, Phys. Rev. D, 69, 083503
Benson B. A., et al., 2013, ApJ, 763, 147
Bertschinger E., Jain B., 1994, ApJ, 431, 486
Beutler F., et al., 2011, MNRAS, 416, 3017
Bhattacharya S., Heitmann K., White M., Lukić Z., Wagner C., Habib S., 2011, ApJ, 732, 122
Bocquet S., Saro A., Dolag K., Mohr J. J., 2016, Mon. Not. Roy. Astron. Soc., 456, 2361
Boehringer H., et al., 2004, Astron. Astrophys., 425, 367
Cataneo M., et al., 2015, Phys. Rev. D, 92, 044009
Cataneo M., Rapetti D., Lombriser L., Li B., 2016, JCAP, 1612, 024
Clifton T., Ferreira P. G., Padilla A., Skordis C., 2012, Phys. Rep., 513, 1
Cooke R. J., Pettini M., Jorgenson R. A., Murphy M. T., Steidel C. C., 2014, ApJ, 781, 31
Copeland E. J., Sami M., Tsujikawa S., 2006, International Journal of Modern Physics D, 15, 1753
Corasaniti P. S., Achitouv I., 2011, Phys. Rev. Lett., 106, 241302
Creminelli P., D'Amico G., Norena J., Vernizzi F., 2009, JCAP, 0902, 018
Creminelli P., D'Amico G., Noreña J., Senatore L., Vernizzi F., 2010a, JCAP, 3, 27
Creminelli P., D'Amico G., Norena J., Senatore L., Vernizzi F., 2010b, JCAP, 1003, 027
Cui W., Baldi M., Borgani S., 2012, MNRAS, 424, 993
Dalal N., Dore O., Huterer D., Shirokov A., 2008, Phys. Rev., D77, 123514
Das S., et al., 2014, J. Cosmology Astropart. Phys., 4, 14
De Felice A., Tsujikawa S., 2010, Living Rev. Rel., 13, 3
Despali G., Giocoli C., Angulo R. E., Tormen G., Sheth R. K., Baso G., Moscardini L., 2016, Mon. Not. Roy. Astron. Soc., 456, 2486
Ebeling H., Edge A. C., Bohringer H., Allen S. W., Crawford C. S., Fabian A. C., Voges W., Huchra J. P., 1998, MNRAS, 301, 881
Ebeling H., Edge A. C., Mantz A., Barrett E., Henry J. P., Ma C. J., van Speybroeck L., 2010, MNRAS, 407, 83
Hannestad S., 2005, Phys. Rev., D71, 103519
Hojjati A., Linder E. V., 2016, Phys. Rev. D, 93, 023528
Holder G., Haiman Z., Mohr J., 2001, Astrophys. J., 560, L111
Howlett C., Lewis A., Hall A., Challinor A., 2012, JCAP, 1204, 027
Hu W., Eisenstein D. J., 1999, Phys. Rev. D, 59, 083509
Hu W., Kravtsov A. V., 2003, ApJ, 584, 702
Jenkins A., Frenk C. S., White S. D. M., Colberg J. M., Cole S., Evrard A. E., Couchman H. M. P., Yoshida N., 2001, Mon. Not. Roy. Astron. Soc., 321, 372
Joyce A., Jain B., Khoury J., Trodden M., 2015, Phys. Rep., 568, 1
Keisler R., et al., 2011, ApJ, 743, 28
Kelly P. L., et al., 2014, MNRAS, 439, 28
Kitayama T., Suto Y., 1996, Astrophys. J., 469, 480
Kopp M., Appleby S. A., Achitouv I., Weller J., 2013, Phys. Rev., D88, 084015
LSST Science Collaboration et al., 2009, preprint, (arXiv:0912.0201)
Lahav O., Lilje P. B., Primack J. R., Rees M. J., 1991, MNRAS, 251, 128
Laureijs R., et al., 2011, preprint, (arXiv:1110.3193)
Lee S., Ng K.-W., 2010, J. Cosmology Astropart. Phys., 10, 028
Lewis A., 2013, Phys. Rev., D87, 103529
Lewis A., Bridle S., 2002, Phys. Rev., D66, 103511
Lewis A., Challinor A., Lasenby A., 2000, Astrophys. J., 538, 473
Lima M., Hu W., 2005, Phys. Rev., D72, 043006
LoVerde M., Miller A., Shandera S., Verde L., 2008, JCAP, 0804, 014
Lombriser L., Slosar A., Seljak U., Hu W., 2012, Phys. Rev. D, 85, 124038
Maggiore M., Riotto A., 2010, ApJ, 711, 907
Majumdar S., Mohr J. J., 2003, Astrophys. J., 585, 603
Mana A., Giannantonio T., Weller J., Hoyle B., Hütsi G., Sartoris B., 2013, MNRAS, 434, 684
Mantz A., Allen S. W., Ebeling H., Rapetti D., 2008, MNRAS, 387, 1179
Mantz A., Allen S. W., Rapetti D., Ebeling H., 2010a, MNRAS, 406, 1759
Mantz A., Allen S. W., Ebeling H., Rapetti D., Drlica-Wagner A., 2010b, MNRAS, 406, 1773
Mantz A. B., Allen S. W., Morris R. G., Rapetti D. A., Applegate D. E., Kelly P. L., von der Linden A., Schmidt R. W., 2014, MNRAS, 440, 2077
Mantz A. B., et al., 2015, MNRAS, 446, 2205
Mantz A. B., et al., 2016, Mon. Not. Roy. Astron. Soc., 463, 3582
Martel H., Shapiro P. R., 1999, ArXiv Astrophysics e-prints,
Matarrese S., Verde L., 2008, Astrophys. J., 677, L77
Meyer S., Pace F., Bartelmann M., 2012, Phys. Rev. D, 86, 103002
Nakamura T. T., Suto Y., 1997, Prog. Theor. Phys., 97, 49
Navarro J. F., Frenk C. S., White S. D. M., 1996, ApJ, 462, 563
Pace F., Waizmann J.-C., Bartelmann M., 2010, MNRAS, 406, 1865
Pace F., Batista R. C., Del Popolo A., 2014, MNRAS, 445, 648
Padmanabhan N., Xu X., Eisenstein D. J., Scalzo R., Cuesta A. J., Mehta K. T., Kazin E., 2012, MNRAS, 427, 2132
Perlmutter S., et al., 1999, Astrophys. J., 517, 565
Planck Collaboration et al., 2014, A&A, 571, A15
Press W. H., Schechter P., 1974, ApJ, 187, 425
Rapetti D., Allen S. W., Mantz A., Ebeling H., 2010, MNRAS, 406, 1796
Rapetti D., Blake C., Allen S. W., Mantz A., Parkinson D., Beutler F., 2013, MNRAS, 432, 973
Reichardt C. L., et al., 2012, ApJ, 755, 70
Riess A. G., et al., 1998, Astron. J., 116, 1009
Riess A. G., et al., 2011, ApJ, 730, 119
Rozo E., et al., 2010, ApJ, 708, 645
Rozo E., Rykoff E. S., Becker M., Reddick R. M., Wechsler R. H., 2015, MNRAS, 453, 38
Rykoff E. S., et al., 2014, ApJ, 785, 104
Rykoff E. S., et al., 2016, Astrophys. J. Suppl., 224, 1
Sartoris B., Borgani S., Fedeli C., Matarrese S., Moscardini L., Rosati P., Weller J., 2010a, MNRAS, 407, 2339
Sartoris B., Borgani S., Fedeli C., Matarrese S., Moscardini L., Rosati P., Weller J., 2010b, MNRAS, 407, 2339
Sartoris B., et al., 2016, Mon. Not. Roy. Astron. Soc., 459, 1764
Schmidt F., Vikhlinin A., Hu W., 2009a, Phys. Rev. D, 80, 083505

Schmidt F., Lima M. V., Oyaizu H., Hu W., 2009b, Phys. Rev., D79, 083518
Shandera S., Mantz A., Rapetti D., Allen S. W., 2013, J. Cosmology Astropart. Phys., 8, 004
Sheth R. K., Tormen G., 1999, MNRAS, 308, 119
Slosar A., Hirata C., Seljak U., Ho S., Padmanabhan N., 2008, JCAP, 0808, 031
Story K. T., et al., 2013, ApJ, 779, 86
Suzuki N., et al., 2012, ApJ, 746, 85
Tinker J., Kravtsov A. V., Klypin A., Abazajian K., Warren M., Yepes G., Gottlöber S., Holz D. E., 2008, ApJ, 688, 709
Tinker J. L., Robertson B. E., Kravtsov A. V., Klypin A., Warren M. S., Yepes G., Gottlöber S., 2010, ApJ, 724, 878
Truemper J., 1993, Science, 260, 1769
Vikhlinin A., et al., 2009, ApJ, 692, 1060
Weller J., Lewis A. M., 2003, MNRAS, 346, 987
Zentner A. R., 2007, International Journal of Modern Physics D, 16, 763
Zuntz J., et al., 2015, Astron. Comput., 12, 45
von der Linden A., et al., 2014, MNRAS, 439, 2

This paper has been typeset from a TEX/LATEX file prepared by the author.